

GT2014-26413

PREDICTION OF THE AERO-ACOUSTIC PERFORMANCE OF OPEN ROTORS

Dale E. Van Zante

NASA Glenn Research Center
Cleveland, OH, USA

Edmane Envia

NASA Glenn Research Center
Cleveland, OH, USA

ABSTRACT

The rising cost of jet fuel has renewed interest in contra-rotating open rotor propulsion systems. Contemporary design methods offer the potential to maintain the inherently high aerodynamic efficiency of open rotors while greatly reducing their noise output, something that was not feasible in the 1980's designs. The primary source mechanisms of open rotor noise generation are thought to be the front rotor wake and tip vortex interacting with the aft rotor. In this paper, advanced measurement techniques and high-fidelity prediction tools are used to gain insight into the relative importance of the contributions to the open rotor noise signature of the front rotor wake and rotor tip vortex. The measurements include three-dimensional particle image velocimetry of the intra-rotor flowfield and the acoustic field of a model-scale open rotor. The predictions provide the unsteady flowfield and the associated acoustic field. The results suggest that while the front rotor tip vortex can have a significant influence on the blade passing tone noise produced by the aft rotor, the front rotor wake plays the decisive role in the generation of the interaction noise produced as a result of the unsteady aerodynamic interaction of the two rotors. At operating conditions typical of takeoff and landing operations, the interaction noise level is easily on par with that generated by the individual rotors, and in some cases is even higher. This suggests that a comprehensive approach to reducing open rotor noise should include techniques for mitigating the wake of the front rotor as well as eliminating the interaction of the front rotor tip vortex with the aft rotor blade tip.

INTRODUCTION

Open Rotors demonstrated significant fuel burn advantage compared to turbofans in 1980's era ground and flight tests (1, 2). Blade designers of the time were not able to optimize for both high aerodynamic efficiency and low noise due to limitations of the design and analysis tools of that time. This led to compromises in aerodynamic efficiency in order to meet the noise regulation requirements for a product.

Current open rotor efforts make extensive use of modern three-dimensional computational fluid dynamics (CFD) and computational aeroacoustics (CAA) tools to produce designs that are both high-efficiency and low-noise (3-5). Additionally, computational methods have been used to further investigate the mechanisms of open rotor noise generation in order to develop rules for low-noise blade designs. Much of this type of work has employed notional blade designs and blade counts, since realistic blade geometries tend to be highly proprietary and not available to the public. Recent examples of this type of work include Danner, et. al (6), where unsteady CFD simulations were analyzed to identify specific aerodynamic mechanisms that lead to open rotor noise generation. Peters and Spakovszky (7) used aero and acoustic simulation tools to associate various blade regions with specific noise generation mechanisms, though their choices of blade regions are somewhat arbitrary. In addition to establishing the important role of 3D blade aerodynamics, results from these analyses confirmed already established conclusions that rotor-rotor spacing and aft rotor tip clipping are effective noise reduction tools. As noted by Brandvik, et al (8), angle of attack effects influence the optimum tip clipping and rotor spacing.

In contrast, the work presented here uses realistic high-performance blade geometries with blade counts that are representative of modern open rotor designs. Furthermore, the acoustic source identification methodology used in the present work does not rely on a priori assumptions for associating particular region(s) of the blade to specific noise source(s).

The experimental data used here to establish the validity of the theoretical analysis were acquired as part of a comprehensive research effort funded by the NASA Environmentally Responsible Aviation (ERA) Project. Under the sponsorship of the ERA project, extensive datasets of flowfield and acoustic measurements were acquired for a benchmark blade design called F31/A31 to enable validation and improvement of design/analysis codes for contra-rotating open rotors (9). An important element of that research program was the acquisition of three-component velocity measurements

in the intra-rotor region (i.e., the region between the two rotors) using stereo particle image velocimetry (PIV). Previously, this PIV dataset was used to analyze the front rotor tip vortex trajectory (10). In the present work, the PIV dataset is used to validate flowfield simulation results generated by the NUMECA’s FINE™/Turbo code. The validated CFD computations are then used as input to an acoustic model to predict tone noise produced by the open rotor, which, in turn, is compared with the measured noise results. The goal of this study is to gain insight into the noise generating regions of the blades and to suggest potential noise mitigation approaches for reducing open rotor noise beyond what has been achieved already.

NOMENCLATURE

- Mach Test section free stream Mach number
- β Blade setting angle at 75% radius (degrees)

Subscripts:

- 1, 2 Front, Aft blade
- C Standard Day Corrected

EXPERIMENTAL CONFIGURATIONS

The wind tunnel configurations and the blade set used for the acquisition of aerodynamic, acoustic, and detailed flowfield measurements have been described in detail in Refs. 10-12. An overview of the configurations is provided here for the sake of completeness.

Open Rotor Testbed

The so-called Historical Baseline blade set, F31/A31, is used for all measurements presented in this paper. F31/A31 is representative of early 1990s aero design technology and is optimized for performance without any compromises for lowering its acoustic signature. The front and aft rotor blade counts for F31/A31 are 12 and 10, respectively. The design tip speed of the rotors is 230 m/s (750 ft/s). A side view of the front and the aft blades is shown in Figure 1. Geometric parameters are given in Table 1.

Table 1: F31/A31 Geometric Parameters	
F31 Diameter	0.652 m (25.662 inches)
A31 Diameter	0.630 m (24.794 inches)
Diameter Ratio (Aft Rotor/Front Rotor)	0.966
Front Rotor Blade Count	12
Aft Rotor Blade Count	10
Blade Spacing to Front Rotor Diameter Ratio	0.31

The F31/A31 aerodynamic and acoustic measurements were acquired in the NASA Glenn Research Center 9-foot by 15-foot Low Speed Wind Tunnel (9x15 LSWT) using the refurbished Open Rotor Propulsion Rig (ORPR). Figure 2 shows the ORPR installed in the 9x15 test section with the

traversing microphone system that was the primary acoustic acquisition tool for this test. Test section freestream conditions were set using a rake mounted on the test section ceiling at an axial location near the rotor plane. Data presented here are standard day corrected to the test section static temperature as is the convention for propellers.

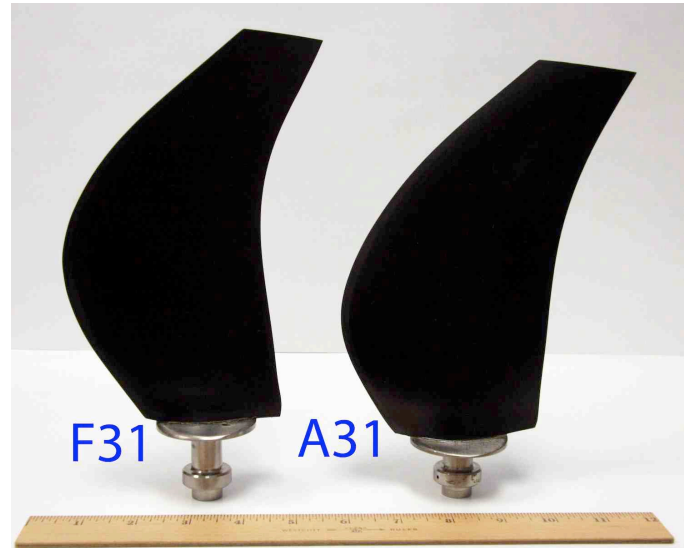


Figure 1: The Historical Baseline blade set, F31/A31.

The primary rotor performance instrumentation was rotating force balances in each rotor hub. The maximum force balance capabilities were ~1,910 N (430 lbf) of thrust and ~745 N-m (550 ft-lbf) of torque. The thrust and torque values are accurate to within 1.0% of force level as determined from check loads of the balances installed in the rotor hubs on the rig. Additionally, the rotor balance thrust values were corrected for pressure-area forces on the rotor disks beneath the flow path and tare drag on the hub contour as determined from measurements with no rotor blades. Details are given in Refs. 5 and 11. Signals were transmitted from the rotating frame to the stationary reference frame with a digital telemetry system.

Acoustic measurements were acquired at a sideline distance of 1.524 m (5 ft) at 18 stops along the traverse track which correspond to 18 sideline geometric angles spanning a range from roughly 18 degrees to 140 degrees with 0 degrees denoting the upstream direction and 180 degrees the downstream direction. The microphone signal was digitized at 200 kHz for 15 seconds per stop. Spectra were then generated using a 2¹⁴ point FFT resulting in a frequency bin width of 12.2 Hz. Details of the acoustic processing, instrument corrections, atmospheric corrections, etc. are discussed in Ref. 12. The accuracy of the acoustic measurement system is ±1 dB.

Performance and acoustic data were acquired at two blade setting angles corresponding to the nominal takeoff (NTO) and approach conditions, at several rotor speeds, multiple angles of attack, and at two different test section Mach numbers. For the purposes of this paper, the focus is on a subset of the test data corresponding to the NTO blade setting angles, six tip speeds,

zero angle of attack, and one Tunnel Mach number. The blade setting angles considered are $\beta_1 = 40.1$ degrees and $\beta_2 = 40.8$ degrees. The range of speeds is listed in Table 2 and includes the nominal design tip speed of 6436 RPM at NTO down to a low part speed of 4620 RPM. Note that the test matrix considered here includes only the equal RPM cases. Furthermore, the RPMs indicated are corrected speeds.

Case	Rotor 1 RPM	Rotor 2 RPM
1	6436	6436
2	6303	6303
3	6068	6068
4	5551	5551
5	5268	5268
6	4620	4620



Figure 2: The F31/A31 Open Rotor installed in 9x15 LSWT. Traversing microphone and its track are seen on the left side.

Stereo PIV Setup

Three-component velocities were measured using the stereo PIV technique for the intra-rotor region. To permit an unobstructed view, the lasers were mounted above the test section and the cameras were in the test section wall as shown in Figure 3. The cameras and lasers were set on three independent translation tracks to measure a series of planes from near the hub to the outboard region of the rotor tips. The light sheet was clipped in the axial dimension at the lower spans by a motorized aperture. The radial spacing of the planes was variable with increased resolution near the blade tip. Figures 4 and 5 show the data volume and measurement locations. The flow was seeded far upstream of the test section using Vicount smoke generators which generated condensed mineral oil droplets in the range of 0.2-0.3 μm in diameter at high volumes. There was no noticeable buildup of mineral oil

on the blade surfaces during the elapsed time to acquire the PIV data.

Extensive PIV system calibrations were performed and multi-step image processing applied to obtain the highest quality and best spatial resolution velocity vector maps possible. See Ref. 10 for details of the PIV processing. To keep the total data acquisition time reasonable, the measurements were synchronized to the forward rotor position only. That is when any of the forward rotor blades was in the correct position, and the laser/camera system was ready to fire, an image pair would be acquired. Blade to blade differences in front rotor geometry or blade setting angle thus appear as ‘turbulence’ in the ensemble averages. The aft rotor position is arbitrary, thus it is assumed that the upstream influence of the aft rotor potential field is minimal. The aft rotor potential field influence would also appear as ‘turbulence’ in the ensemble average velocity field. This point will be discussed further in the Intra-Rotor Velocity Field Comparisons section below.

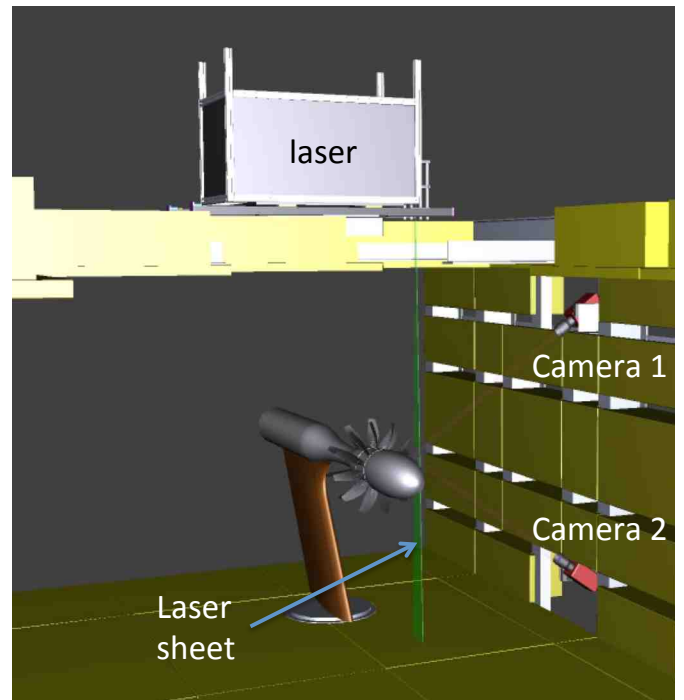


Figure 3: Stereo PIV configuration in the 9x15 LSWT with the Open Rotor Propulsion Rig.

Sequences of 400 velocity vector maps were acquired at each measurement station and were ensemble-averaged to provide first and second order statistics over the entire measurement plane. The wind tunnel has very low free stream turbulence and thus experience has shown that an average of 400 vector maps is adequate to converge the velocity statistics given the other potential sources of uncertainty. All of the processed PIV data were placed in the model coordinate system to facilitate comparison with CFD predictions. The final processed velocity vector maps had an in-plane spatial resolution of 1.43 mm in both directions in the measurement

plane. The velocity measurements have an accuracy of better than 1% of full scale.

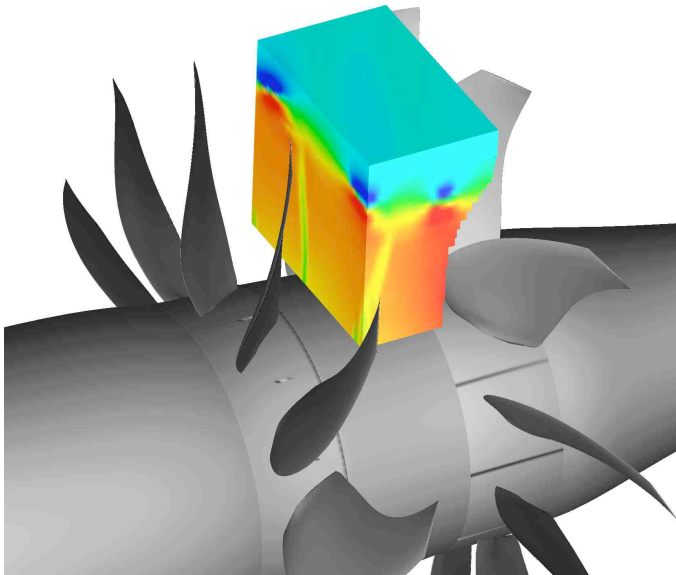


Figure 4: Perspective view of the PIV intra-rotor measurement region.

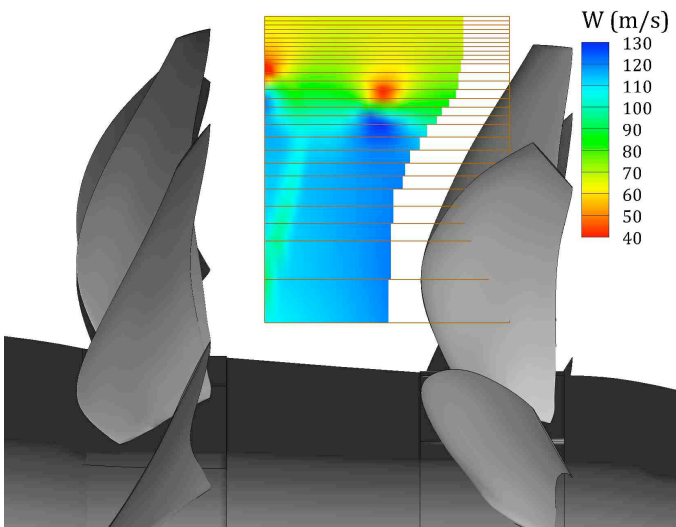


Figure 5: PIV measurement planes (a total of 30 horizontal planes). Note that the spanwise and streamwise extent of the measurement planes get smaller as one moves down the span towards the hub.

The PIV data were acquired for multiple blade setting angles and speeds, but the focus here is on the one condition corresponding to the NTO at 6303 RPM, which is highlighted in Table 2.

COMPUTATIONAL SETUP

The computational tool used for the aerodynamic calculations in this work is the commercial CFD software package FINE™/Turbo developed by NUMECA International. FINE™/Turbo is a turbomachinery CFD simulation software package with integrated meshing and post-simulation analysis tools. It is a structured, multi-block, unsteady Navier-Stokes solver, which offers several solution algorithm choices along with several acceleration strategies. To reduce the computational time requirements for the time-dependent simulations, FINE™/Turbo was run in the nonlinear harmonic (NLH) mode which solves for a finite number of the blade passing frequency harmonic components of the time-dependent solution, but ignores all the other unsteady components (13). For this study, only three loading harmonics were retained to keep the computational cost reasonable. This implies that tones up to the 66th shaft order could be modeled.

The FINE™/Turbo computational domain used in generating the results presented in this paper includes one passage each of the two blade rows and their associated ancillary domains like the spinner, hub, farfield, etc. The total mesh size is slightly over 27.1 million grid points with the farfield boundary set seven tip radii away. The equivalent full-wheel grid for a full unsteady simulation would require almost 300 million grid points. The Spalart-Almaras turbulence model was used in this simulation to best represent the physics of the problem. Further details of the simulation setup are given in Ref. 14. The computational domain is shown in Figure 6.

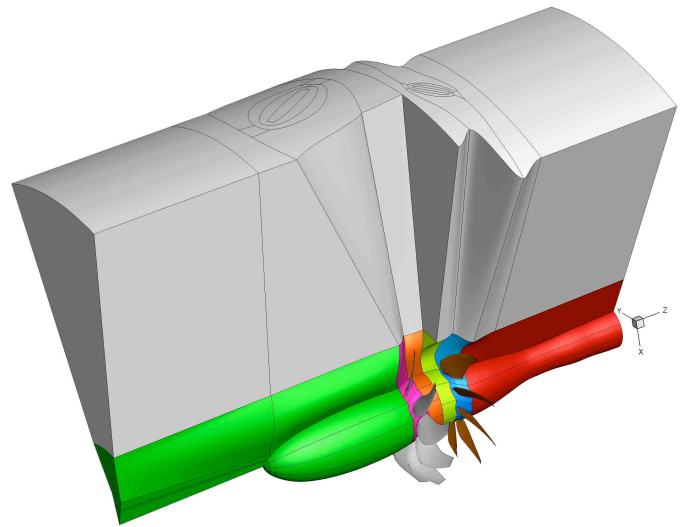


Figure 6: CFD computational domain, which contains 91 computational blocks and 27.1 million grid points.

The acoustic computations were carried out using a NASA code called LINPROP, which is based on a high-blade-count asymptotic approximation of the Ffowcs-Williams Hawkins equation (see Ref. 14 for further detail). The LINPROP code was used to predict the tone noise on a 5-foot (1.524 m)

sideline parallel to the rotational axis of the open rotor. This duplicates the experimental setup in the wind tunnel where the acoustic data were acquired using the traversing microphone. The nacelle geometry, rotor geometry and aerodynamic pressure distributions from the CFD calculation are direct inputs to the LINPROP calculation.

PERFORMANCE AND FLOW FIELD COMPARISONS

To evaluate the accuracy of the CFD simulations, overall performance metrics, such as rotor thrust and torque ratio (i.e., ratio of aft rotor torque to the front rotor torque), are first compared to the numerical results and then more detailed comparisons of the intra-rotor velocity fields follow.

Overall Performance Comparisons

FINETM/Turbo aerodynamic simulations were generated for six rotor speeds that match, on corrected RPM basis, a subset of the conditions from the wind tunnel test. Figure 7 shows the data-prediction comparisons for the total thrust and torque ratio at the corrected speed of 6303 RPM_C. This is the corrected speed for which the PIV data were acquired. The overall predicted thrust values match to better than 1.5% with the measured data. The torque ratio values match to better than 11%. It should be noted that the FINETM/Turbo calculations were true predictions in the sense that no attempt was made to modify the grid, boundary conditions, or operating condition to match a measured parameter.

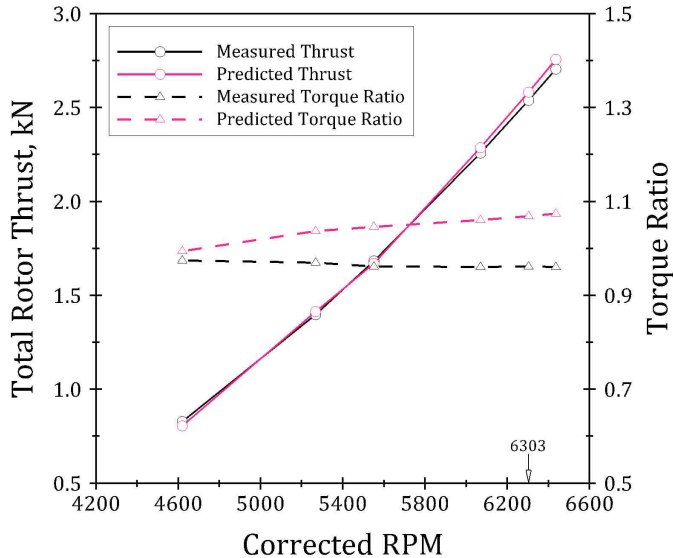


Figure 7. Comparison of measured and predicted total rotor thrust and torque ratio.

Furthermore, the F31/A31 rotor system geometry, which was supplied by GE, is for the top of climb condition. For the purposes of the work presented here, the blades were re-pitched to match the nominal takeoff blade setting angles, but no attempt was made to compute the hot shapes corresponding to the NTO condition. It was expected that the blade shape

differences would be relatively small at least for the condition considered in this paper. Next, the details of the velocity field are compared for the 6303 RPM_C condition.

RPM _C	Thrust, N (lbf)		Torque Ratio	
	Measured	Predicted	Measured	Predicted
6303	2539 (571)	2581 (580)	0.962	1.069

Intra-Rotor Velocity Field Comparisons

The distribution of the axial velocity field is compared at two axial locations in the intra-rotor region as shown in Figure 8. For reference, the aft rotor pitch change axis is at the origin (i.e., 0.0 cm). The forward rotor pitch change axis is at -19.91 cm (-7.84 in). Velocity comparisons are shown at -13.30 cm (-5.25 in) and at -5.70 cm (-2.25 in). The first location is close to the forward rotor trailing edge in order to compare the front rotor wake shape and tip vortex character. The second location is close to the aft rotor leading edge and shows how the wake and tip vortex have evolved before striking the aft rotor.

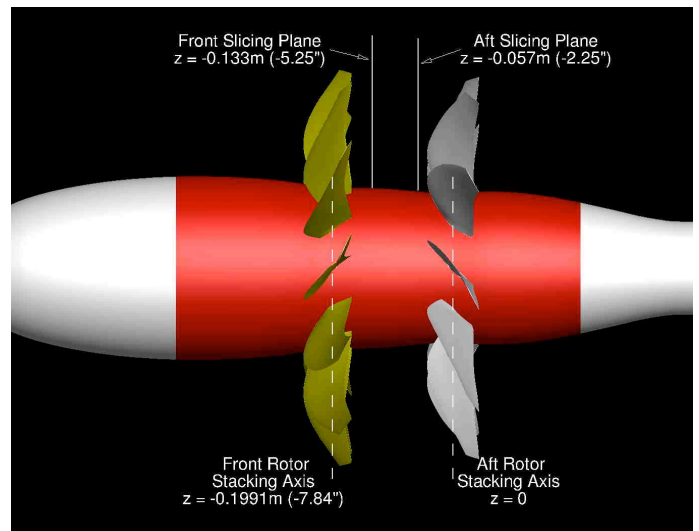


Figure 8: Locations for detailed intra-rotor velocity comparisons.

The predicted axial velocity fields for the full circumference at these two axial planes are shown in Figure 9. Unlike the ensemble-averaged PIV results to be discussed later, the simulated velocity fields are for an instant in time. Figure 9A shows essentially a periodic pattern of the forward rotor wakes and tip vortices 12 times around the circumference. The distribution shows almost no passage-to-passage variations, which implies that the aft rotor potential field influence is quite weak at this location. This conclusion bears out the assumption made in acquiring the PIV data. However, the downstream station distribution, shown Figure 9B, exhibits significant circumferential variation due to the 12 wake/vortex pattern of the front rotor interacting with the potential field of the 10-

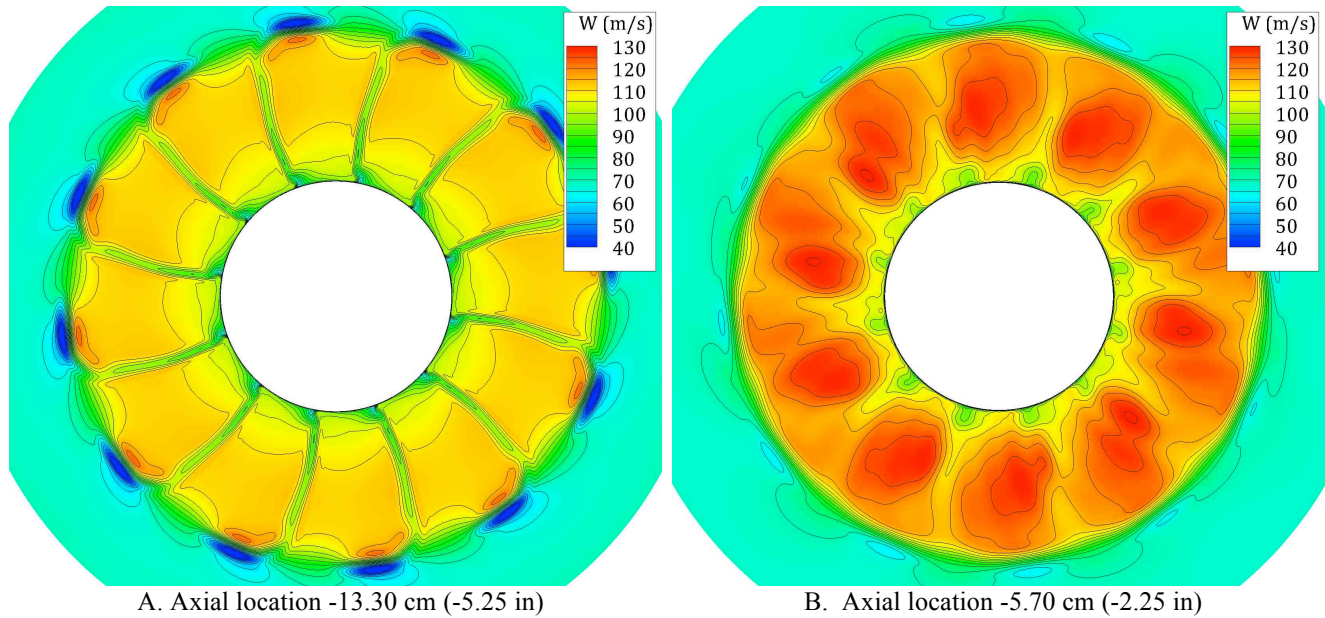


Figure 9: Instantaneous axial velocity (W) contours in two axial planes extracted from the CFD solutions. The left pane shows the results for the axial plane close to the front rotor trailing edge and the right pane shows the results for the plane close to the leading edge of the aft rotor.

bladed aft rotor. The forward rotor wakes are visible as 12 low velocity regions at the inner diameter. However, the image is dominated by 10 higher velocity regions, which are due to the potential field influence of the aft rotor.

In light of these results, the interpretation of the PIV data is crucial for meaningful data-theory comparisons. In the planes near the front rotor, it is expected that the ensemble-averaged PIV maps are effectively equivalent to the instantaneous velocity distributions like that shown in Figure 9A since there are virtually no passage-to-passage variations in the flowfield at these locations. On the other hand, for the planes close to the aft rotor, the PIV maps should be noticeably different from the instantaneous picture like that shown in Figure 9B. That is because the relative position of the front and aft rotor blades is not known at the instant that any of the PIV images was acquired. As such the ensemble average is not phased-locked to any known fixed relative positions of the two rotors. Therefore, since it is not possible to ensemble-average the CFD results in precisely the same manner that the PIV averages were constructed, we carry out a straightforward front rotor phase-locked averaging as an approximation for the sake of comparisons with the PIV data near the aft rotor. This is an average using six passages. Note that given the 12/10 blade counts and the equal front and aft rotor RPMs, the simulated flowfield is periodic in a half-wheel so only half the field needs to be considered in ensemble averaging. For the sake of illustrating the instantaneous variations, some representative ones together with the ensemble average are shown.

Figure 10 shows the velocity comparison at the front axial location. The PIV results show a clearly defined tip vortex in the upper center of the velocity field. Two forward rotor blade wakes are also visible in the velocity field. The CFD results at

the same axial plane show remarkably similar features. Figure 11A shows axial velocity along a radial line that passes through the velocity minimum of the tip vortex in the PIV results (the white dashed line). The identical location was extracted from the CFD solution and plotted for comparison. Note the excellent agreement in the core flow velocity. The PIV results show a larger velocity difference through the vortex. Figure 11B shows a comparison of wake profiles on a constant radius cut (the white curved dashed line). Again, the core flow velocities and wake widths show good agreement. The CFD shows a deeper wake. Overall agreement of absolute values, location and characteristics of flow non-uniformities is quite good at this axial location.

The data/CFD comparison at the downstream location, shown in Figure 12, is more complex. The PIV data in Figure 12A show a diminished, though still distinct, tip vortex and forward rotor blade wakes. Note that the radial extent of the PIV data at that station is limited (recall Figure 5) in order to mitigate the risk of the laser sheet damaging the aft rotor blade. The CFD flow features (Figure 12B) are less distinct. A more revealing comparison is shown in Figure 13, where the CFD results are also averaged though not exactly in the same manner as the PIV data as discussed earlier. Detailed comparisons along a radial line and a constant radius are shown in Figure 13. Both the tip vortex (Figure 13A) and blade wakes (Figure 13B) are more mixed out in the CFD solution compared to the ensemble average PIV data. The three instantaneous velocities from the CFD solution are also shown as dashed lines. The solid magenta lines show the phase-locked average of the CFD results to serve as an approximation to the way the PIV data were generated. While, for the reasons discussed earlier, the comparison would never be exact, it is nonetheless clear that

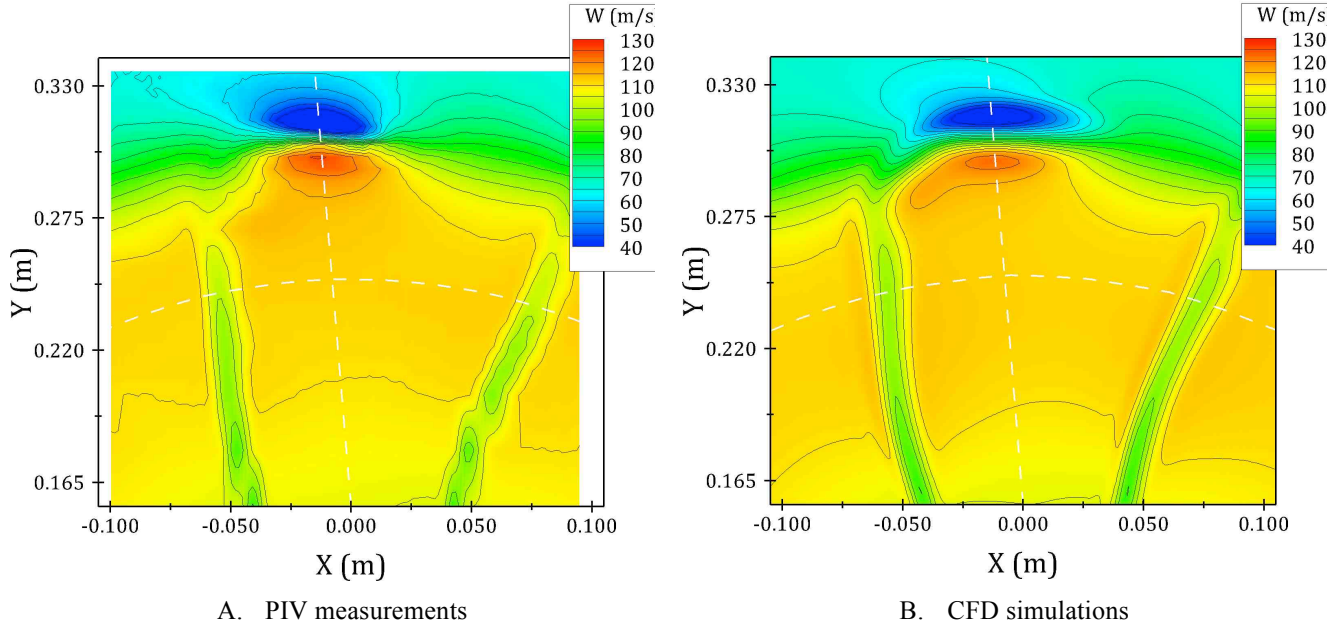


Figure 10: Measured and predicted axial velocity (W) contours in a plane 13.36 cm (5.26 inches) upstream of the aft rotor pitch change axis. Dashed lines show locations of velocity profiles depicted in Figure 11.

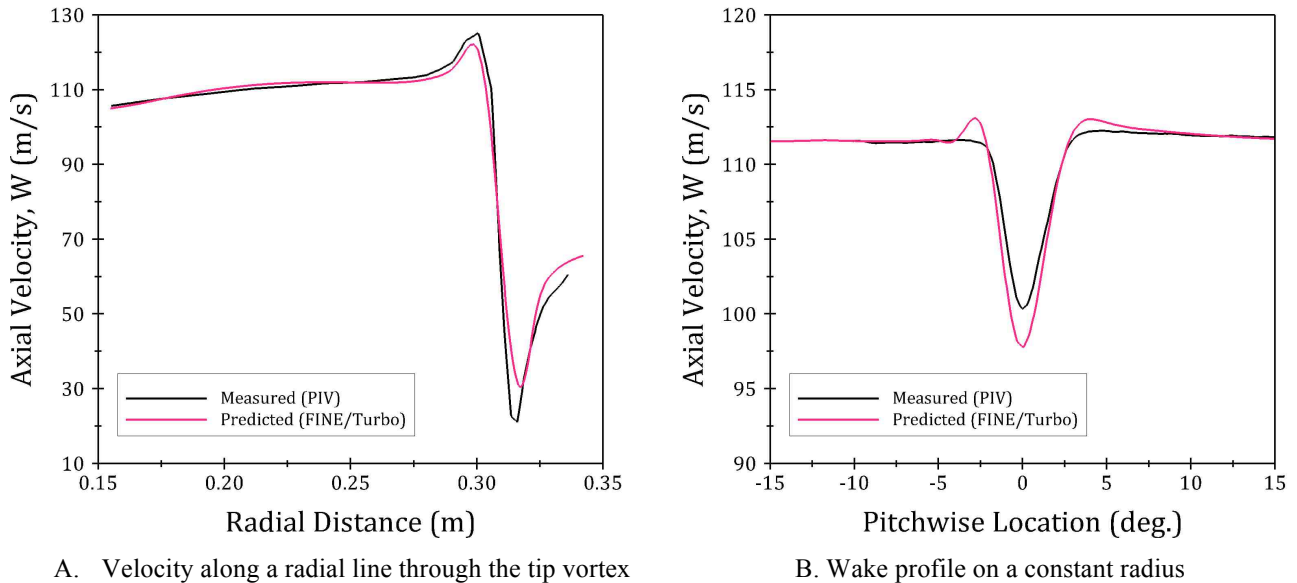


Figure 11: Comparison of measured and predicted axial velocity (W) in a plane 13.36 cm (5.26 inches) upstream of the aft rotor pitch change axis.

the predictions exhibit more dissipation than is seen in the measured data. However, given the limitations of this comparison, and the fact that the data-theory difference is actually small, i.e., about 5% in the maximum wake velocity deficit (see Figure 13B), the agreement is still quite reasonable. In any case, small differences do not have a large impact on the acoustic results, since a 10% change in the aerodynamic input level translates into a 1 dB change in the acoustic level.

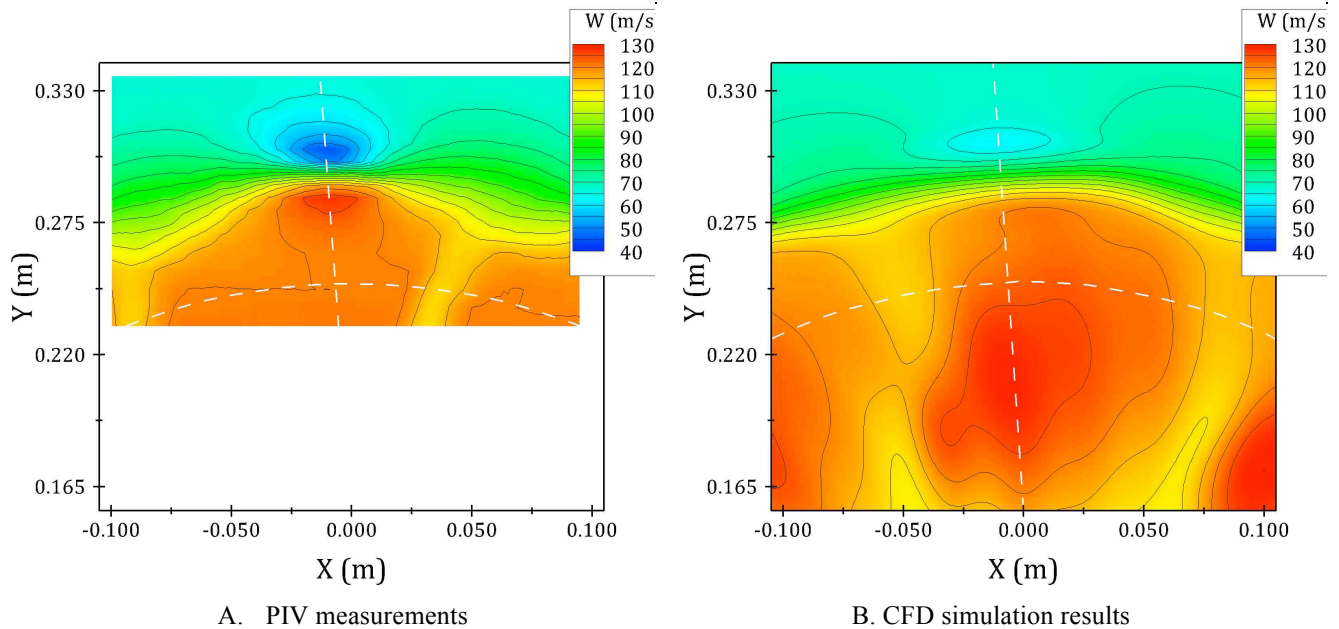


Figure 12: Measured and predicted axial velocity (W) contours in a plane 5.70 cm (2.25 inches) upstream of the aft rotor pitch change axis. Dashed lines show locations of velocity profiles depicted in Figure 13.

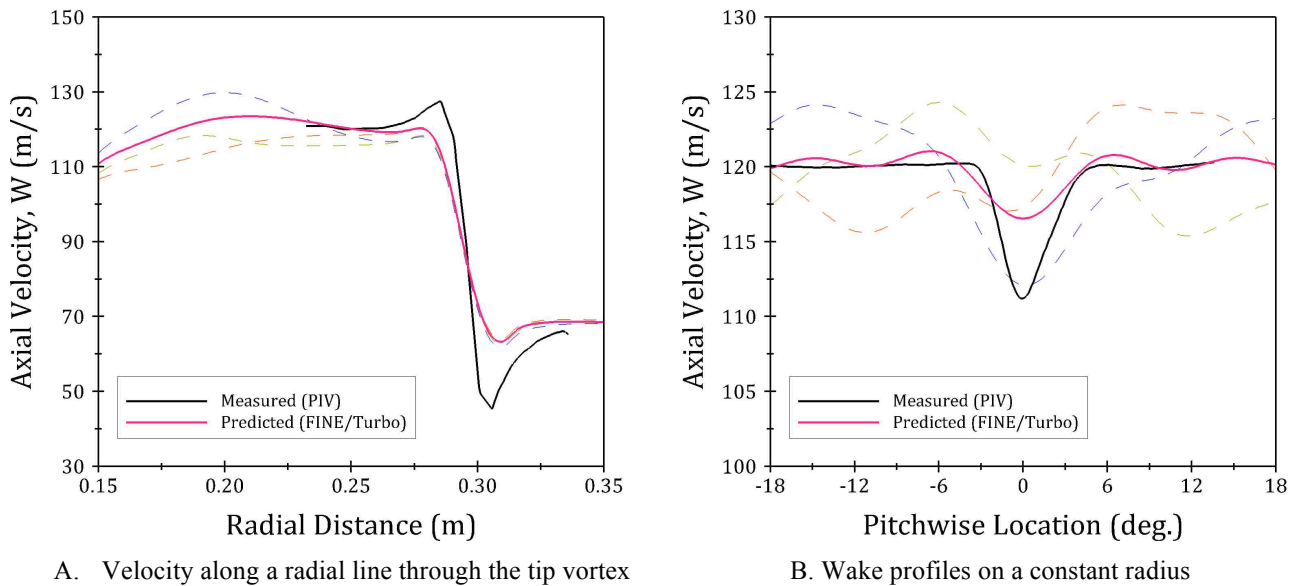


Figure 13: Comparison of measured and predicted axial velocity (W) in a plane 5.70 cm (2.25 inches) upstream of the aft rotor pitch change axis.

ACOUSTIC RESULTS

The blade harmonic loading distributions extracted from the CFD simulations were used as input to the LINPROP code in order to predict the tone spectra of F31/A31 at various conditions. Both individual rotor tones (denoted by $n\text{BPF}_1$ and $n\text{BPF}_2$) as well as interaction tones (denoted by $m\text{BPF}_1 + k\text{BPF}_2$) were computed on the 1.526 meters sideline at a large

number of angles encompassing all of the 18 acoustic measurements locations used in the wind tunnel test. Note that m , n and k in the above expressions are arbitrary integers.

Since open rotor acoustic spectra are rich in tone content, it is useful for the subsequent discussion to show an example of the measured spectra and identify some of the important aspects of the spectrum. Figure 14 shows the measured sound pressure level (SPL) spectrum for F31/A31 at the 6303 RPM_C condition

at the broadside angle of 90 degrees. The abscissa is given in terms of the rotor shaft orders, since it makes the tone identification easier. Recall that F31/A31 has 12 front blades and 10 aft blades and the rotor rotational speeds are equal for the cases considered here. It is typical to have open rotor tones rising well above the broadband level up to the 200th shaft order, but for the sake of clarity only tones up to the 48th shaft order are shown in Figure 14. Tones below the 8th shaft order are contaminated by the rig noise or tunnel background noise and are not shown. The labels identify some of the expected individual rotor tones and interaction tones based on the theory. However, clearly there are more tones in the measured spectrum than indicated by the theory. The preponderance of tones in the measured spectrum is due to the fact that the blades in each rotor are never identical nor can they ever be set in the hub with precisely the same blade setting angles. These imperfections result in the scattering of some of the acoustic energy into shaft orders other than those that would be predicted if the blades in each rotor were identical in every respect. Even small variations in the blades in each rotor destroy the perfect phase relationship assumed by the theory and result in the generation of extraneous tones. This inherent discrepancy should be kept in mind when comparing the theoretical predictions to the measured data. It should also be noted that the number of interaction tones in the spectrum far exceeds that of the individual rotor tones. In fact, for takeoff and approach conditions, the interaction tones levels can be noticeably higher than those of individual rotor tones, a point that is germane to the main thrust of this paper. The importance of this observation will be discussed shortly.

Figure 15 shows the comparison of measured and predicted SPL spectra for the blade passing tones of the front and aft rotors (i.e., BPF_1 & BPF_2) as well as the first interaction tone (i.e., $BPF_1 + BPF_2$) over a range of sideline angles. It should be noted the predicted tone levels are confined to a bin width of zero Hertz while the measured tone levels are spread across multiple frequency bins. Therefore, in order to compare the measured levels to the predicted ones, it was necessary to sum the tone energy in the bins over which the measured tone is spread. Furthermore, where the tone level is close to the broadband level (i.e., less than 6 dB), tone extraction is problematic. That is because it is not clear how much of the energy is due to the tone and how much of it is associated with the underlying broadband level. As such, where the measured tone level is less than 6 dB above the background level, the measured tone level is not plotted. The results in Figure 15 show that the absolute tone levels are not well predicted by the theory primarily as a result of the idealization assumed in both the CFD simulations and the LINPROP acoustic calculations as was discussed earlier. Nevertheless, the trends with the sideline angle are fairly well predicted by the theory. In fact, predicting acoustic trends is often a more useful tool in guiding the design than the absolute levels. Therefore, the authors felt justified in using the LINPROP code to analyze and ultimately identify the dominant noise generating regions of the blade that control the radiated acoustic field. Before reviewing the results of the

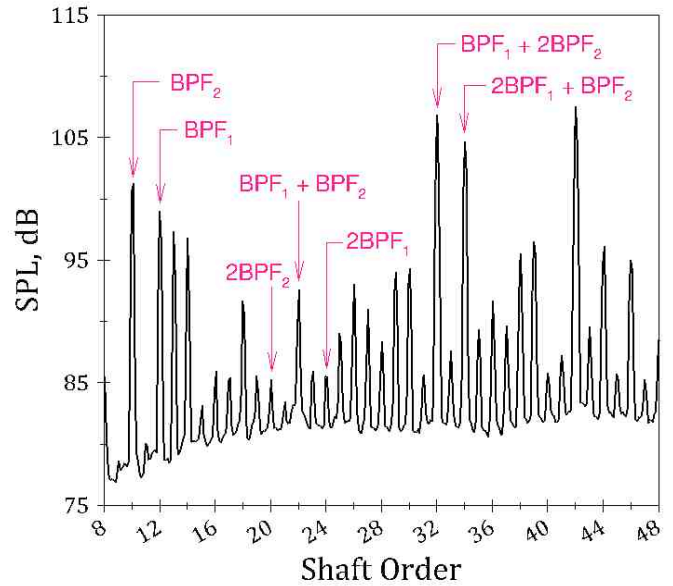


Figure 14: Comparison of absolute tone levels for the first 48 shaft orders at 90 degrees, (i.e., broadside) to the aft rotor for the 6303 RPM_C speed. A few individual rotor tones and some interaction tones are highlighted. The spectrum below the 8th shaft order is contaminated by rig noise and tunnel background noise.

analysis, it is important to elucidate certain aspects of the results in Figure 15.

First, note the clear difference between the directivities of the individual rotor tones and the interaction tones. Whereas the individual rotor tones tend to peak around angles centered on the broadside (i.e., 90 degrees), the interaction tones tend to radiate substantially more towards the upstream and/or downstream directions as compared with the broadside direction. This is seen in the measured data as well as the predictions. It is important to point out that the source of the individual rotor tones is the steady loading on the rotors blades, whereas the source of the interaction tones is the unsteady loading induced on the blades as a result of the aerodynamic coupling between the two rotors. Interestingly, though the steady loading is at least two orders of magnitude larger than the perturbation loading, the substantially higher radiation efficiency of the interaction tones (see Ref. 14) more than compensates for their small source strength thus generating levels that for some interaction tones exceed the individual rotor tones as seen in the example results shown in Figure 14.

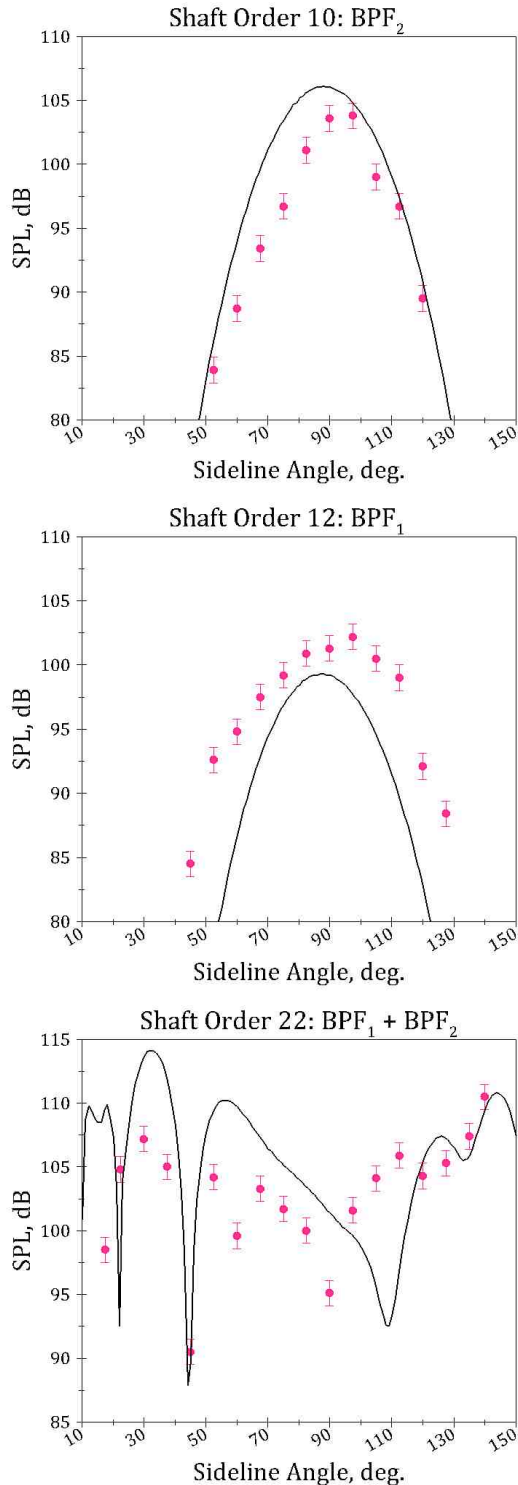


Figure 15: Data-Theory comparisons for the first three principal tones: top BPF_2 , middle BPF_1 , and bottom BPF_1+BPF_2 . Solid lines denote predictions from LINPROP and symbols denote wind tunnel data. Data have a ± 1 dB uncertainty band.

Another noteworthy aspect of the interaction tones is that while both rotors can generate any given interaction tone, the theoretical analysis indicates that the aft rotor contribution tends to be far more substantial than that of the front rotor, typically by a factor of 10. The reason for this behavior is related to the fact that the viscous coupling of the two rotors is far stronger than their potential field coupling as attested to by the discussion of the results in Figure 9. The analysis also indicates that the aft rotor harmonic tones (i.e., $nBPF_2$) are stronger than those of the front rotor (i.e., $nBPF_1$). Taken together these observations substantiate the widely held belief that the aft rotor is the dominant source of open rotor noise and as such has been the focus of noise reduction research.

A substantial portion of open rotor noise reduction research has focused on the tip vortex as the main culprit of aft rotor noise generation. In that vein, the most popular noise reduction approach has been to clip the aft rotor blade tip and/or to modify the front rotor blade tip so as to mitigate the strength of the tip vortex interaction with the aft blade. While this approach has proven successful in reducing open rotor noise, a more potent approach must also consider the importance of the front rotor wake impingement on the aft rotor. That is because the wake not only substantially influences the aft rotor steady loading, it also controls its unsteady loading. As such it has a significant influence on the aft rotor tones as well as the interaction tones. As was mentioned in the introduction, attempts have been made in past to quantify the relative importance of the contributions from the tip vortex and blade wake to the overall noise of the open rotor (e.g., Ref. 7). However, these analyses have been somewhat ad hoc in their choices for assessing the relative importance of the tip vortex versus the blade wake.

In contrast, in the present study, the question of the relative importance of the tip vortex and blade wake has been addressed by a systematic analysis of the contributions to the noise field from the aft rotor blade span without any a priori choices about which portion of the blade may be important for a given source. The results from this analysis are summarized in Figures 16 through 19 for select (but representative) aft rotor tones and some important interaction tones. The selected tones are BPF_2 , $2BPF_2$, BPF_1+BPF_2 , BPF_1+2BPF_2 . Each figure includes a pair of plots with the top portion showing the predicted SPL sideline directivity of the tone and the bottom portion a contour plot of the contribution to the sideline SPL directivity from the various regions on the blade. Specifically, the contour shows the change in tone level as a function of aft rotor blade percent span that is included in the noise calculations. The contour level is referenced to the full-span tone level, so that the relative SPL (i.e., ΔSPL) is zero when the entire span is taken into account.

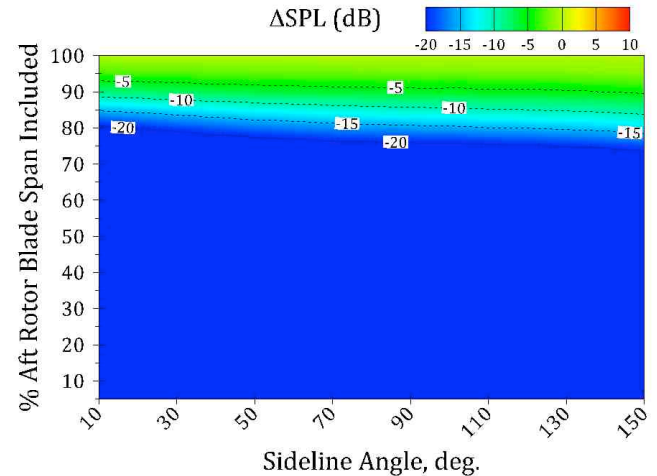
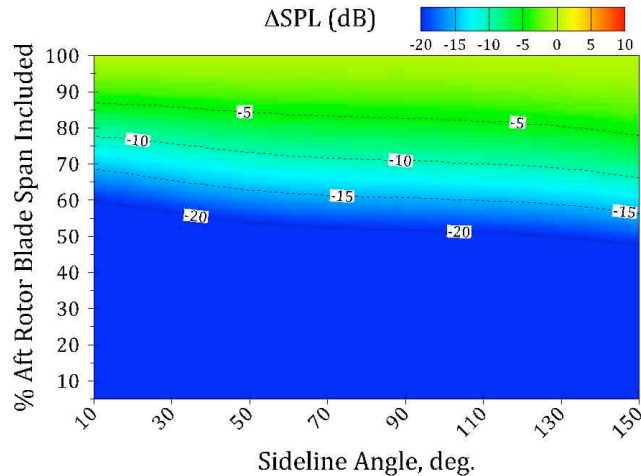
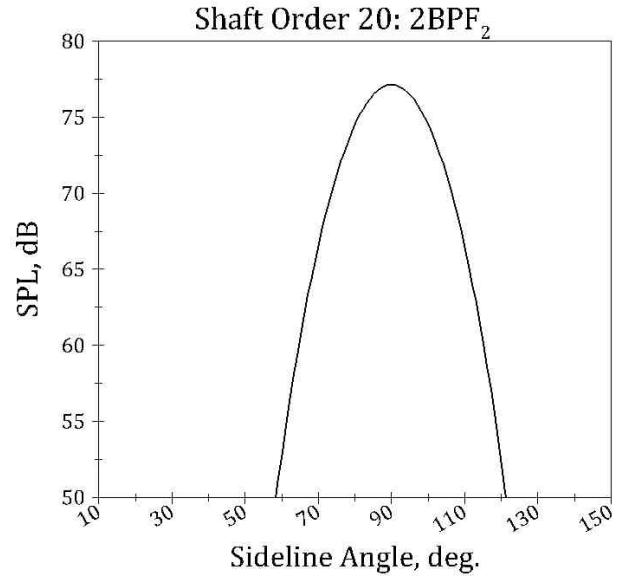
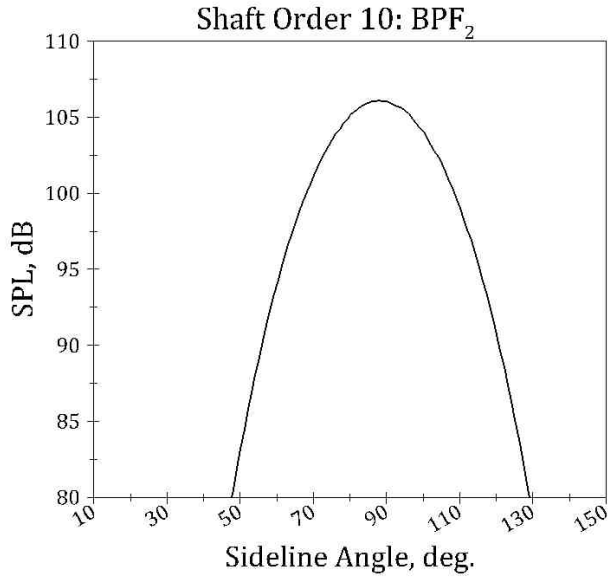


Figure 16: Change in BPF₂ tone SPL as a function of aft rotor blade percent span included in noise calculations relative to the full-span tone level.

Figure 17: Change in 2BPF₂ tone SPL as a function of aft rotor blade percent span included in noise calculations relative to the full-span tone level.

It should be noted that the partial blade loading levels have been corrected for the loss of thrust that would be experienced with a partial blade by raising the loading level on the partial blade by multiplying the loads by an amount equal to the thrust ratio $T_{full\ span} / T_{part\ span}$, where $T_{full\ span}$ is the aft rotor thrust when the entire span is taken into account, and $T_{part\ span}$ is when only part span is considered. This has the effect of increasing the affected tone dB level by $10 \log_{10} (T_{full\ span} / T_{part\ span})$. The correction is negligible near the tip, but is around 16 dB when very small portions of the span are considered. The correction does not change the behavior observed in the contour plots, but has the effect of bunching up the contours. Finally, since only the steady loads contribute to blade thrust, no correction has been applied to the unsteady loading. As a result, only the

levels of rotor tones have been adjusted, but not the interaction tone levels.

The contour levels shown in Figure 16 through 19 should then be interpreted as follows. Take Figure 16 for example. If one takes into account the contributions from the first 75% of the aft blade span to the BPF₂ tone level, one finds that the resulting sideline noise level will be approximately 10 dB less than the full span level across the entire sideline angle range. Therefore, it quickly becomes clear that the last 25% or so of the aft blade span contributes about 90% of the radiated level of the BPF₂ tone since dB is a logarithmic scale. An even smaller portion of the outboard section of the blade is needed (about 10%) to generate most of the 2BPF₂ tone level on the sideline as see in Figure 17. By contrast, the inboard region of the blade

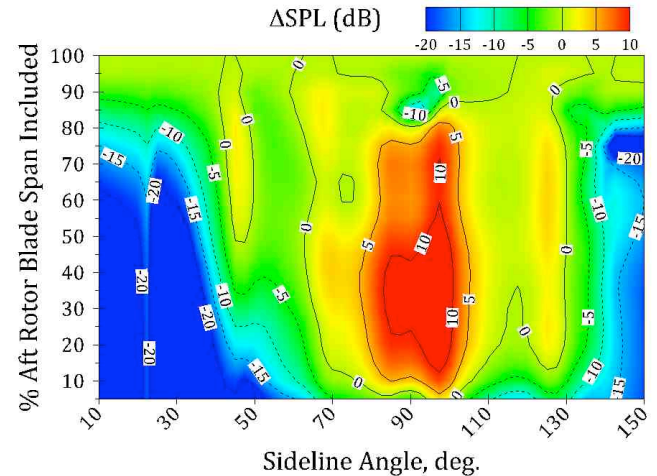
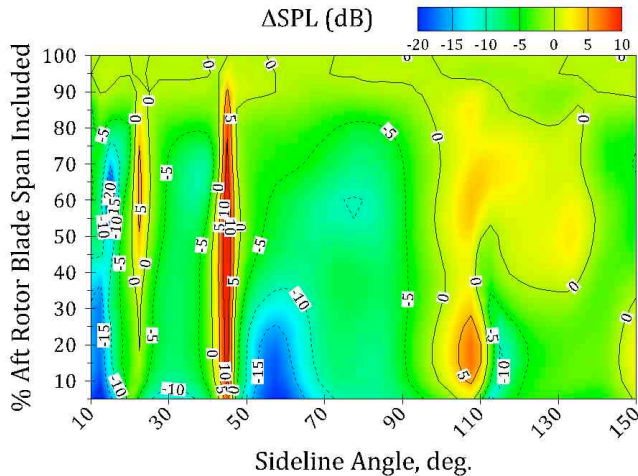
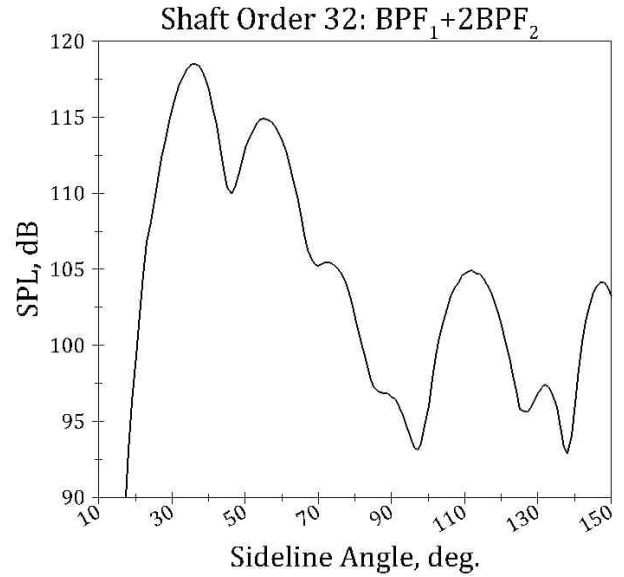
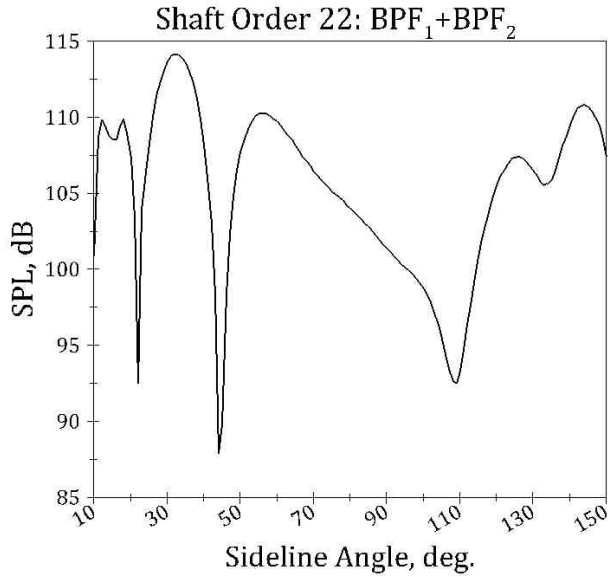


Figure 18: Change in BPF_1+BPF_2 tone SPL as a function of aft rotor blade percent span included in noise calculations relative to the full-span tone level.

Figure 19: Change in BPF_1+2BPF_2 tone SPL as a function of aft rotor blade percent span included in noise calculations relative to the full-span tone level.

contributes only a minute fraction (about 1%) to the levels of the BPF_2 and $2BPF_2$ tones below about 60% of the span. The same story holds for the higher harmonics of the BPF_2 tone. This result would appear to substantiate the view that clipping the aft rotor tip (say, to about 80% span) should have a measurable affect on reducing the total open rotor tone noise (in this case about 10 dB for BPF_2 tone level and 15 dB for $2BPF_2$ tone). However, this would be misleading.

As it can be clearly seen in Figures 18 and 19, the behavior of the interaction tones BPF_1+BPF_2 and BPF_1+2BPF_2 is radically different. Instead of the outboard portion of the blade being the main source of noise, the entire span is involved in generating the tone level as evidenced by the complex Δ SPL contour patterns for these tones. In fact, given positive contour

levels associated with some partial blade spans, it becomes clear that the radiated acoustic field of an interaction tone is a complex amalgam of the contributions from the entire span with no one particular region holding sway over the tone level. In fact, if the blade is clipped injudiciously, the interaction tone level could actually increase owing to reduced interference caused by the missing blade portion. This is most clear for the BPF_1+2BPF_2 tone between 80 and 100 degrees on the sideline. For example, if the blade were clipped by 20%, the tone level would go up by about 5 dB. Given the measured tone levels shown in Figure 14, such clipping would result in a substantial net increase in the noise because, while the levels of the BPF_2 and $2BPF_2$ tones would decrease, the increase in the level of BPF_1+2BPF_2 tone would more than offset these benefits.

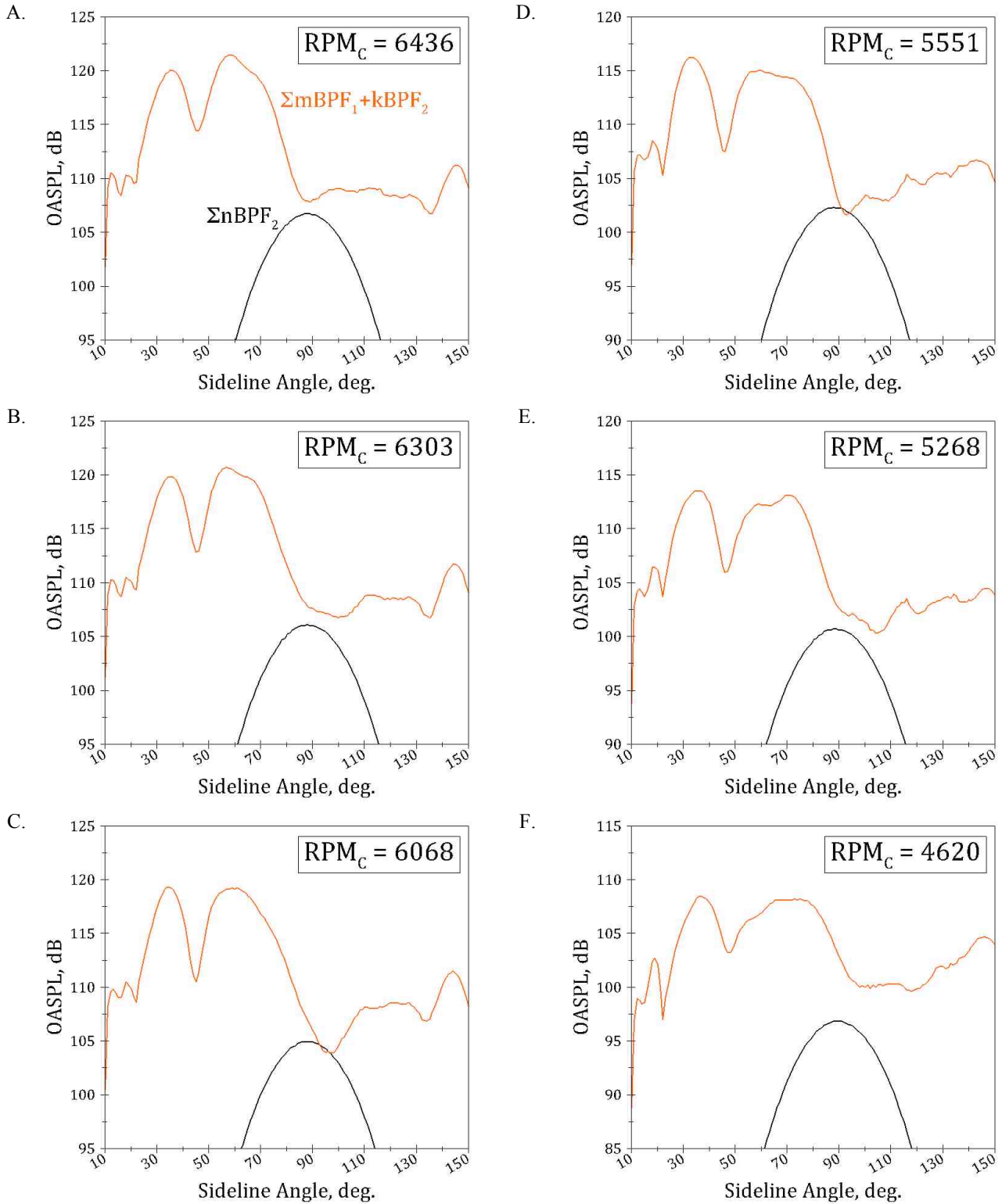


Figure 20. Variations of predicted overall sound pressure level (OASPL) as a function of the sideline angle for all aft rotor tones (i.e., $\Sigma nBPF_2$) and interaction tones (i.e., $\Sigma mBPF_1 + kBPF_2$) considered in this study. Results are shown for highest tip speed considered (i.e., 6436 RPM_c) to the lowest (4620 RPM_c).

To further illustrate the importance of the interaction tones at operating conditions like takeoff and approach, in Figure 20 the predicted sideline directivity of the overall sound pressure level (OASPL) for all the aft rotor tones, i.e., $\sum nBPF_2$, and the OASPL for all the interaction tones, i.e., $\sum mBPF_1 + kBPF_2$, are plotted for various tip speed conditions investigated in this study. The OASPL for the aft rotor tones (shown in black) includes five harmonics, but the BPF_2 level dominates the total. For the interaction tones (shown in orange), the OASPL includes nine tones, which are all the interaction tones that could be calculated given that the aerodynamic simulations had only three loading perturbations included (see the discussion in the COMPUTATIONAL SETUP section). It is clear from these results that the interaction tones make the dominant contribution to the overall tone noise signature of the open rotor for all the speeds considered in this study.

DISCUSSION

In view of the acoustic results shown in Figures 16 through 20, it is the main conclusion of this study that any open rotor noise reduction strategy that ignores the importance of the interaction tones may not only be sub-optimal, it may actually lead to inadvertent noise level increases. That is because, while the rotor tones and their harmonics are controlled by the outboard portion of the span, the interaction tones receive far more distributed contributions from the blade span. In fact, the distribution is not even uniform in that loss of a portion of the blade could lead to higher noise levels at some sideline angles. Therefore, noise control strategies involving the clipping of the aft blade tip or modifying the front rotor blade tips to reduce the strength of the interaction of the front blade tip vortex with the aft blade tips are only effective in reducing the $nBPF_2$ tone levels. Such approaches, however, would do little to reduce the interaction tones, which are controlled by the wake of the front rotor. Therefore, to substantially reduce open rotor tone noise beyond what has been achieved through blade tip clipping or similar approaches requires complementary techniques involving judicious control of the wake of the front rotor. An example of such an approach is the so-called trailing edge blowing (15). Furthermore, wake management strategies should be predicated on optimization studies that maximize noise reductions for the target tones while minimizing noise increases for the other tones. It should be noted that spacing increases could also reduce wake strength, but it is likely that the necessary spacing increases would be impractical.

CONCLUSIONS

Three-dimensional PIV measurements have been used to validate FINETM/Turbo CFD simulations of a contra-rotating open rotor system. Detailed comparisons of the measured and predicted velocity fields show good agreement for the evolution of the forward rotor wake/tip vortex characteristics. Surface pressure distributions from the CFD simulations were used as input to the LINPROP acoustic code to predict the associated open rotor tone noise spectra.

While the absolute noise level predictions have proven to be difficult, the sideline directivity trends were shown to be quite reasonable. These results provided confidence in the predictions so that they can be used to gain better insight into the radiated fields by the various open rotor tones. Insights that are not available from the measured data. In particular, the results from the LINPROP prediction code indicate that, in contrast to the individual rotor tone levels which are controlled by the blade outboard portion, the interaction tones levels are controlled by the entire span suggesting that blade wakes are more important than the tip vortices in setting the interaction tone levels. This insight in turn suggests that a comprehensive approach to open rotor noise reduction should involve not only tip vortex interaction mitigation, but also blade wake mitigation to enable further noise reduction for open rotor systems.

ACKNOWLEDGMENTS

This work was supported by the NASA Environmentally Responsible Aviation and Fixed Wing Projects. The PIV data were acquired and processed by Mark Wernet, Randy Locke, Adam Wroblewski and Gary Clayo. The acoustic measurements were acquired by David Elliott and David Stephens, all technical research staff at NASA Glenn Research Center.

REFERENCES

1. Hager, R.D. and Vrabel, D., "Advanced Turboprop Project," NASA SP-495, 1988.
2. Bowles, Mark D., "The 'Apollo' of Aeronautics, NASA's Aircraft Energy Efficiency Program," NASA SP-2009-574, 2010.
3. Khalid, S. Arif, Wojno, John P., Breeze-Stringfellow, Andy, Lurie, David P., Wood, Trevor H., Ramakrishnan, Kishore, and Paliath, Umesh, "Open Rotor Designs for Low Noise and High Efficiency," GT2013-94736, presented at ASME Turbo Expo 2013, San Antonio, TX, June 3-7, 2013.
4. Zachariadis, Alexios, Hall, Cesare, and Parry, Anthony B., "Contrarotating Open Rotor Operation for Improved Aerodynamics and Noise at Takeoff," ASME Journal of Turbomachinery, Vol. 135, No. 3, pages 031010-1 to 10, May 2013.
5. Van Zante, Dale E., Collier, Fayette, Orton, Arthur, Khalid, S. Arif, Wojno, John P., and Wood, Trevor H., "Progress in Open Rotor Propulsors: The FAA/GE/NASA Open Rotor Test Campaign," to be published in the Aeronautical Journal, Royal Aeronautical Society, 2014.
6. Danner, Florian, Kendall-Tory, Christofer, and Kau, Hans-Peter, "Aerodynamic Origin of Rotor-Rotor Interaction Noise From Unducted Propulsors," GT2013-95572, presented at ASME Turbo Expo 2013, San Antonio, TX, June 3-7, 2013.
7. Peters, Andreas and Spakovszky, Zoltan S., "Rotor Interaction Noise in Counter-Rotating Propfan Propulsion Systems," ASME Journal of Turbomachinery, Vol. 134, No. 1, pp. 011002 1-12, 2012.
8. Brandvik, Tobias, Hall, Cesare and Parry, Anthony B., "Angle-of-Attack Effects on Counter-Rotating Propellers at

Take-off,” GT2012-69901, presented at ASME Turbo Expo 2012, Copenhagen, Denmark, June 11-15, 2012.

9. Van Zante, Dale E., “The NASA Environmentally Responsible Aviation Project/General Electric Open Rotor Test Campaign,” AIAA-2013-0415, 51st AIAA Aerospace Sciences Meeting, Grapevine, TX, 7-10 January, 2013.

10. Van Zante, Dale E. and Wernet, Mark P., “Tip Vortex and Wake Characteristics of a Counterrotating Open Rotor,” AIAA-2012-4039, 48th AIAA/ASME/SAE/ASEE Joint Propulsion Conference, Atlanta, GA, 29 July – August 1, 2012.

11. Van Zante, Dale, Gazzaniga, John, Elliott, David, and Woodward, Richard, “An Open Rotor Test Case: F31/A31 Historical Baseline Blade Set,” ISABE-2011-1310, Gothenburg, Sweden, September 2011.

12. Elliott, David M., “Initial Investigation of the Acoustics of a Counter Rotating Open Rotor Model With

Historical Baseline Blades in a Low Speed Wind Tunnel,” AIAA 2011-2760, 17th AIAA/CEAS Aeroacoustics Conference, Portland, Oregon, June 2011.

13. He, L. and Ning, W., “Efficient Approach for Analysis of Unsteady Viscous Flows in Turbomachines”, AIAA Journal, Vol. 36, No. 11, pp. 2005-2011, 1998.

14. Envia, Edmane, “Open Rotor Aeroacoustic Modelling,” NASA TM-2012-217740, Conference on Modelling Fluid Flow, Budapest, Hungary, September 4-7, 2012.

15. Woodward, Richard P.; Fite, E. Brian; Podboy, Gary G., “Noise Benefits of Rotor Trailing Edge Blowing for a Model Turbofan,” NASA TM-2007-214666, AIAA 2007-1241, 45th AIAA Aerospace Sciences Meeting and Exhibit; 8-11 Jan. 2007.